Chapter 3.5
Decentralized Control of Aerial Manipulators based on a momentum-based estimator

Fabio Ruggiero

Abstract Aerial Robotic Manipulators can be controlled either in a *centralized* or *decentralized* way. This Part of the book addresses the latter option, in which the aerial platform and the arm are controlled separately in a robust way to counteract the reciprocal disturbances. An estimator of such disturbances, based on the momentum of the system and acting on the unmanned aerial vehicle, is designed. Experiments validate the approach.

1 Brief introduction

A *decentralized* approach might be suitable in those circumstances where the dynamics of the robotic arm attached to the UAV is not fast enough to compensate for the position errors of the aerial platform, and/or the arm does not allow a torque control modality. In this context, the term decentralized is used to indicate the case where the UAV and the robotic arm are seen as two separate independent entities: the effect of the movements of the arm is seen as an external disturbance by the UAV and vice versa. Therefore, control issues for the two entities are addressed separately.

On the one hand, robust control of the sole robot manipulator is well-established in the literature [9], and it is out of the scope of this chapter. On the other hand, the control of the single UAV with standard techniques may be not sufficient to deal with the presence of the moving arm. As a matter of fact, in addition to the standard issues caused by neglecting relevant aerodynamics terms within the dynamic model and the underactuation of the floating platform (in single-direction thrust UAVs like the quadrotors), suitable control laws must be designed to counteract the destabilizing movements of the arm. For this reason, suitable disturbance observers/estimators and robust controllers are thus adequately designed and superimposed to the existing controllers. A short literature review reveals a multilayer architecture to control multirotor UAVs equipped with a servo robot arm [6], where the momentum-based estimator presented in [4, 5] is employed to compensate for unwanted aerodynamic

Table 14 Symbols used to derive the momentum-based estimator of external wrenches.

Definition	Symbol
Configuration space for the roll-pitch-yaw angles $\boldsymbol{\eta}_b$	$\mathcal{Q}_\eta$
Vector of the generalized moments	$\boldsymbol{\rho} \in \mathbb{R}^6$
Estimated wrench	$\hat{\mathbf{w}}_e$
Current wrench	$\mathbf{w}_e$
Diagonal matrix of transfer functions	$\boldsymbol{\Sigma}(s) \in \mathbb{C}^{6 \times 6}$
Degree of the estimator	$r \in \mathbb{N}$
Coefficients of the Hurwitz polynomial included within the i-th transfer function of the estimator	$c_j, \ j = 0, \dots, r-1$
Positive definite diagonal gain matrices	$\mathbf{K}_i, \ i = 1, \dots, r$

effects and the arm dynamics. A variable parameter integral backstepping controller improves the results obtained by a simple PID-based controller for the UAV [3]. A AROMA composed of a helicopter and a fully actuated redundant robot arm (a Kuka LWR with 7 DoFs) does not show coupling effects when the center of gravity of the arm is moved in the lateral plane of the helicopter: forcing the movement of the arm in that direction, thanks to its intrinsic redundancy, exhibits a coupling between the UAV and the manipulator only at a kinematic level [2].

In this chapter, the momentum-based estimator presented in [4, 5] is revised and generalized. Experiments in which such an estimator is tested bolster the efficiency of the decentralized approach.

2 Momentum-based estimator of external wrenches

The dynamic model (7) is employed to design the described approach. The following assumptions are considered.

- The aerial vehicle does not pass through the singularities. The allowable configuration space for the yaw-pitch-roll angles $\boldsymbol{\eta}_b$ is thus $\mathcal{Q}_\eta = \{ \boldsymbol{\eta}_b \in \mathbb{R}^3 \mid \theta \neq \frac{\pi}{2} + k\pi, \ k = \dots, -1, 0, 1, \dots \}$.
- The unknown forces $\mathbf{f}_e(\cdot)$ and moments $\boldsymbol{\tau}_e(\cdot)$ depend only on the time variable t, and they are continuously differentiable with respect to it. The Euclidean norms of the unknown forces and moments and the Euclidean norms of the related time derivatives are all bounded.

A broad discussion about the employed assumptions can be found in [7].

The generalized momentum vector $\boldsymbol{\rho} \in \mathbb{R}^6$ of the system (7) can be defined as

$$\boldsymbol{\rho} = \begin{bmatrix} m\mathbf{I}_3 & \mathbf{O}_3 \\ \mathbf{O}_3 & \mathbf{M}(\boldsymbol{\eta}_b) \end{bmatrix} \begin{bmatrix} \dot{\mathbf{p}}_b \\ \dot{\boldsymbol{\eta}}_b \end{bmatrix}, \tag{134}$$

where $\mathbf{I}_n \in \mathbb{R}^{n \times n}$ and $\mathbf{O}_n \in \mathbb{R}^{n \times n}$ are the identity and zero matrices, respectively. Considering the expression (7b), the following property holds [9]

$$\dot{\boldsymbol{\eta}}_b^{\mathrm{T}} \left(\dot{\mathbf{M}}(\boldsymbol{\eta}_b) - 2\mathbf{C}(\boldsymbol{\eta}_b, \dot{\boldsymbol{\eta}}_b) \right) \dot{\boldsymbol{\eta}}_b = 0. \tag{135}$$

From the expressions of $\mathbf{M}_b(\boldsymbol{\eta}_b)$ and $\mathbf{C}(\boldsymbol{\eta}_b, \dot{\boldsymbol{\eta}}_b)$ and the above property, it is possible to prove that the following expressions holds

$$\dot{\mathbf{M}}(\boldsymbol{\eta}_b, \dot{\boldsymbol{\eta}}_b) = \mathbf{C}(\boldsymbol{\eta}_b, \dot{\boldsymbol{\eta}}_b) + \mathbf{C}(\boldsymbol{\eta}_b, \dot{\boldsymbol{\eta}}_b)^{\mathrm{T}}. \tag{136}$$

By using (7) and (136), the time derivative of the generalized momentum vector (134) is

$$\dot{\boldsymbol{\rho}} = \begin{bmatrix} -f_z \mathbf{R}_b(\boldsymbol{\eta}_b)\mathbf{e}_3 + \mathbf{f}_e(t) + m\mathbf{g} \\ \mathbf{Q}(\boldsymbol{\eta}_b)^{\mathrm{T}}\boldsymbol{\tau}_u^b + \boldsymbol{\tau}_e(t) + \mathbf{C}(\boldsymbol{\eta}_b, \dot{\boldsymbol{\eta}}_b)^{\mathrm{T}}\dot{\boldsymbol{\eta}}_b \end{bmatrix}. \tag{137}$$

The goal of the proposed estimator is to achieve a linear relationship between the estimated external wrench and its time derivatives with the real one. In the Laplace domain, this is achieved through the following expression

$$\hat{\mathbf{w}}_e(s) = \boldsymbol{\Sigma}(s)\mathbf{w}_e(s), \tag{138}$$

where $s \in \mathbb{C}$ is the complex variable in the Laplace domain, $\hat{\mathbf{w}}_e = \begin{bmatrix} \hat{\mathbf{f}}_e^{\mathrm{T}} & \hat{\boldsymbol{\tau}}_e^{\mathrm{T}} \end{bmatrix}^{\mathrm{T}} \in \mathbb{R}^6$ is the estimated wrench, and $\boldsymbol{\Sigma}(s) \in \mathbb{C}^{6 \times 6}$ is a diagonal matrix of transfer functions whole i-th element is in the form

$$\Sigma_i(s) = \frac{k_0}{s^r + c_{r-1}s^{r-1} + \cdots + c_1 s + c_0}, \tag{139}$$

where $c_i > 0$, $i = 0, \ldots, r-1$ are coefficients assembling a Hurwitz polynomial, and $r \geq 1$ is the desired degree of the estimator. Hence, each component of the estimated external wrench is a filtered estimate of the real one.

To get (139) component-wise in (138), the following recursive estimator is designed in the time domain

$$\boldsymbol{\gamma}_i(t) = \mathbf{K}_i \int_0^t \left(-\hat{\mathbf{w}}_e(\sigma) + \boldsymbol{\gamma}_{i-1}(\sigma) \right) \mathrm{d}\sigma, \text{ if } i = 2, \ldots, r, \tag{140a}$$

$$\boldsymbol{\gamma}_1(t) = \mathbf{K}_1 \left(\boldsymbol{\rho}(t) - \int_0^t \left(\hat{\mathbf{w}}_e(\sigma) - \mathbf{d}(\sigma) \right) \mathrm{d}\sigma \right), \tag{140b}$$

where $\hat{\mathbf{w}}_e = \boldsymbol{\gamma}_r$ and

$$\mathbf{d}(t) = \begin{bmatrix} -f_z \mathbf{R}_b(\boldsymbol{\eta}_b)\mathbf{e}_3 + m\mathbf{g} \\ \mathbf{Q}(\boldsymbol{\eta}_b)^{\mathrm{T}}\boldsymbol{\tau}_u^b + \mathbf{C}(\boldsymbol{\eta}_b, \dot{\boldsymbol{\eta}}_b)^{\mathrm{T}}\dot{\boldsymbol{\eta}}_b \end{bmatrix}$$

and it is assumed that $\boldsymbol{\rho}(0) = \boldsymbol{\gamma}_i(0) = 0$, with $i = 1, \ldots, r$, while $\mathbf{K}_i \in \mathbb{R}^{6 \times 6}$ are positive definite diagonal matrices. Considering (7) and (136), the dynamics of the recursive momentum-based estimator proposed in (140) is

$$\sum_{i=0}^{r} \left(\prod_{j=r}^{i+1} \mathbf{K}_j \right) \hat{\mathbf{w}}_e^{(i)} = \prod_{i=1}^{r} \mathbf{K}_i \mathbf{w}_e, \tag{141}$$

where $\hat{\mathbf{w}}_e^{(i)} = \boldsymbol{\gamma}_{r-i}$ denotes the i-th time derivative of the external wrench estimate, with the convention $\hat{\mathbf{w}}_e^{(0)} = \hat{\mathbf{w}}_e$ and $\prod_{j=r}^{r+1} \mathbf{K}_j = \mathbf{I}_6$. The expression (141) is equivalent to the 6 transfer functions in (138).

The quantities required to compute $\hat{\mathbf{w}}_e$ are the UAV orientation $\boldsymbol{\eta}_b$ and the related time derivative $\dot{\boldsymbol{\eta}}_b$, the vehicle translational velocity $\dot{\mathbf{p}}_b$, the commanded input torques $\boldsymbol{\tau}_u^b$, the thrust f_z and the knowledge about the UAV inertia matrix $\mathbf{I}_b$ and mass m. The quantities $\boldsymbol{\eta}_b$ and $\dot{\boldsymbol{\eta}}_b$ can be retrieved by the on-board IMU sensor, while $\dot{\mathbf{p}}_b$ can be estimated by using GPS and/or visual data. The thrust f_z and the input torques $\boldsymbol{\tau}_u^b$ are given by the implemented controller. The UAV inertia $\mathbf{I}_b$ and mass m should be instead known a-priori. Notice that no inversion of the inertia matrix $\mathbf{M}(\boldsymbol{\eta}_b)$ is required, and also no knowledge about the absolute position $\mathbf{p}_b$ of the UAV is needed.

3 Experimental tests

The proposed estimator can be inserted in many existing model-based control architecture to counteract the effects of the unmodeled dynamics, without changing their structure and the tuned gains. Two different case studies are considered bolstering the concept. In the former, the momentum-based estimator is inserted into the passivity-based controller described in [5]. In the latter, the estimator is inserted into a multilayer architecture, having as core a classical hierarchical architecture made of PID-based controllers, to control an aerial manipulator [6].

3.1 Case study 1

Taking into account a VToL UAV, the rotational dynamics is faster than the translational dynamics. For this reason, a hierarchical architecture is usually implemented by separating the two. The approach proposed in [5] designs a closed-loop mechanical impedance behavior for the translational part; while the rotational part does not rely upon an exact cancellation of the mathematical model. Robustness is thus conferred to the attitude part. The described momentum-based estimator of the external wrench is employed to compensate for wind, aerodynamics effects not included within the mathematical model, unknown payload, battery consumption, physical interaction, and so on. The designed passivity-based controller for the aerial vehicle sees only the estimation error as a perturbation, and not the whole external wrench, resulting in a less demanding actuation. Mathematical details are out of the scope of this chapter and can be consulted by the reader in [5]. Following, the obtained experimental results are discussed.

An Asctech Pelican quadrotor is employed in the tests described in this first case study. Both the controller and the estimator have been implemented onboard at 100 Hz on an ATOM CPU with a patched RTAI real-time kernel UBUNTU OS.

An OptiTrack system tracks the position and the attitude of the aerial vehicle. The linear and angular velocities are computed numerically. A ground station made up of a personal computer with UBUNTU OS is in charge of the WiFi communication between the OptiTrack systems and the aerial vehicle, as well as of the operator telemetry.

The mass m and the inertia $\mathbf{I}_b$ of the vehicle that have been considered in the controller are 1.2 kg and $\mathrm{diag}(3.4, 3.4, 4.7) \cdot 10^{-3}$ kgm^2, respectively. The vehicle parameters in (6) are $d = 0.21$ m, $C_T = 1.8 \cdot 10^{-5}$ Ns^2/rad^2 and $C_Q = 8 \cdot 10^{-7}$ Nms^2/rad^2. Regarding the estimator, instead, the degree is chosen as $r = 2$, while the gains are tuned to $\mathbf{K}_1 = 14\mathbf{I}_6$ and $\mathbf{K}_2 = 3.9\mathbf{I}_6$.

3.1.1 Test A.

In a first test, the quadrotor tracks three times a given circular trajectory with a constant speed of 0.5 m/s. The circle is planned in the horizontal plane at a constant altitude of 1 m. The radius of the planned circle is of about 0.83 m. Take-off and landing phases are not shown in the provided plots.

The comparison between the norms of the position error in the case of the passivity-based control with and without the compensation of the external wrench (e.g., unmodeled dynamics) is shown in Fig. 102(a). The same comparison is depicted in Fig. 102(b) for the norms of the attitude error. From the two mentioned pictures it is possible to notice that the passivity-based control alone is able to track the circle successfully. The average position error norm is of about 5 cm whose acceptability relies on the particular task. However, the performance is substantially improved by using the designed estimator. The norm of the position error decreases to less than 2 cm.

The estimated external wrench is depicted in Fig. 102(e) and Fig. 102(f), from which it is possible to notice that some uncertainties are present in the considered dynamic model of the UAV. For instance, the considered inertia matrix might be inaccurate; while the estimated force along the vertical axis z might be an indicator about either a wrong mass or the commanded thrust is not entirely equal to the actual one.

The commanded propellers inputs are represented in Fig. 102(c) and Fig. 102(d).

3.1.2 Test B.

In a second test, the same circular trajectory of the previous test is addressed. Nevertheless, an external load was physically added to the aerial vehicle, while it is not considered in the controller. In detail, after the take-off, a pendulum is attached to the frame of the quadrotor through a hook (see Fig. 103), at a position far about 15 cm from the vertical axis of the vehicle. The pendulum weights about 0.15 kg and has a length of 0.21 m.
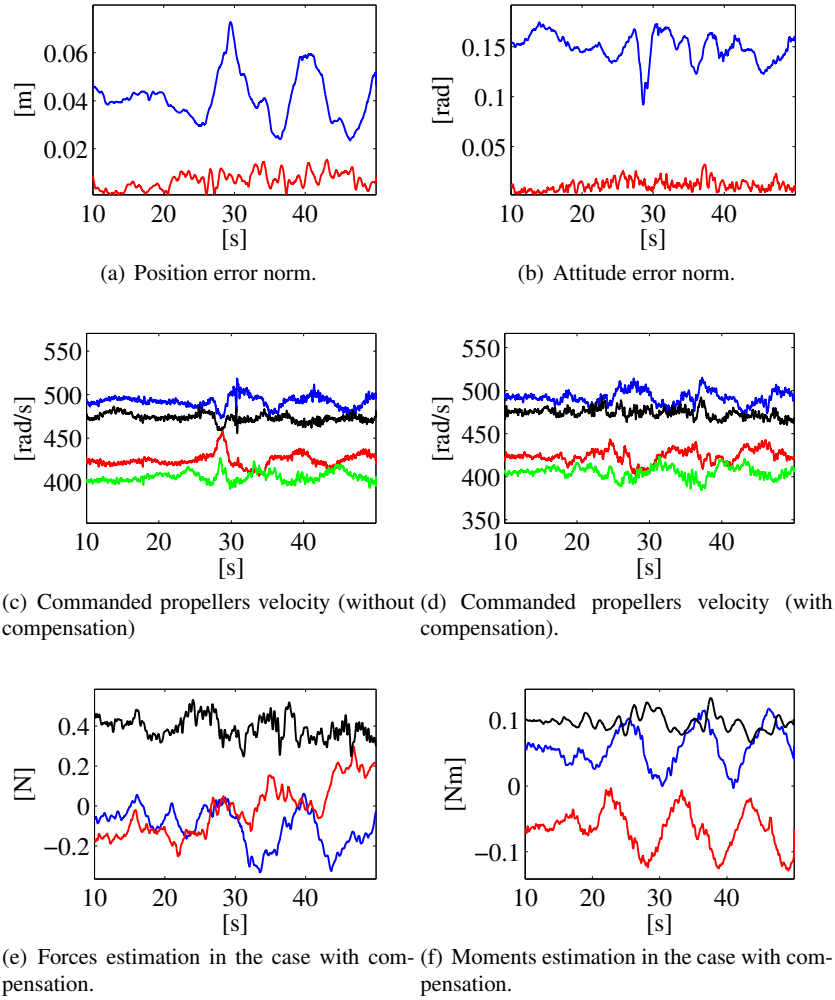
(a) Position error norm.

(b) Attitude error norm.

(c) Commanded propellers velocity (without compensation)

(d) Commanded propellers velocity (with compensation).

(e) Forces estimation in the case with compensation.

(f) Moments estimation in the case with compensation.

Fig. 102 Case study 1. Test A. Subfigure (a) shows the position error norm, while subfigure (b) illustrates the attitude error norm. In both subfigures the legend is: in blue, the case without compensation of external wrench and unmodeled dynamics; in red, the case with compensation. Subfigures (c) and (d) show the commanded propellers velocity without and with compensation, respectively. For these plots, the legend is: blue, propeller 1; red, propeller 2; black, propeller 3; green, propeller 4. In case of compensation, subfigures (e) and (f) depict the estimated forces and moments, respectively. For subfigure (e) the legend is: in blue, the estimated force along the x axis; in red, the y axis; in black, the z axis. The legend for subfigure (f) is instead: in blue, the estimated moment around the x axis; in red, the y axis; in black, the z axis.

The effect of the additional load is visible in Fig. 104(e) and Fig. 104(f), where the estimated force reflects both the presence of the additional mass of the pen-
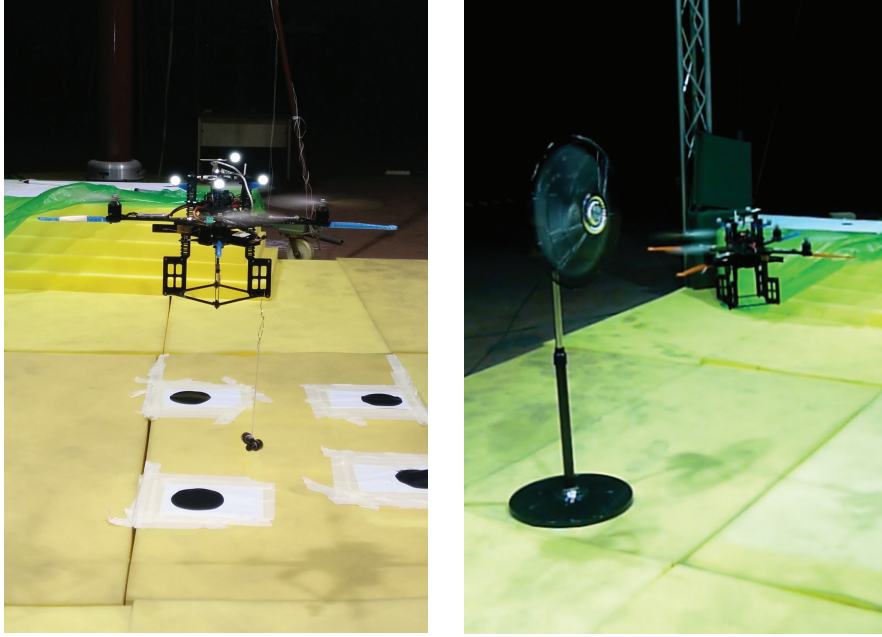
Fig. 103 Left: quadrotor with the attached pendulum. Right: quadrotor in front of the fan.

dulum and the estimation of unmodeled terms. Moreover, comparing Fig. 102(f) with Fig. 104(f) it is possible to notice the effect of the oscillations of the pendulum during the circular trajectory causes the presence of significant unknown moments. These disturbances affect the performance of the controller. Namely, in the passivity-based control alone, the average position error norm is about 9 cm (see Fig. 104(a)), while the average attitude error norm is about 10 degrees (see Fig. 104(b)). However, in any case, such control exhibits robust properties in the presence of unmodelled and unpredicted effects. The compensation provided by the estimator undoubtedly increases the performance as it possible to see in Fig. 104(a) and Fig. 104(b).

The commanded propellers inputs are represented in Fig.s 104(c)-104(d).

3.1.3 Test C.

In a third test, the quadrotor is subject to an external disturbance caused by the fan shown in Fig. 103. The fan is placed at about 1.1 m from the ground and at a distance of about 20 cm from the aerial vehicle in the horizontal plane. After the take-off, the quadrotor reaches first the altitude of 0.6 m, and then 1.8 m passing in front of the fan. Then, the aerial vehicle decreases its altitude again to 0.6 m passing again through the wind flow generated by the fan. Finally, the quadrotor reaches
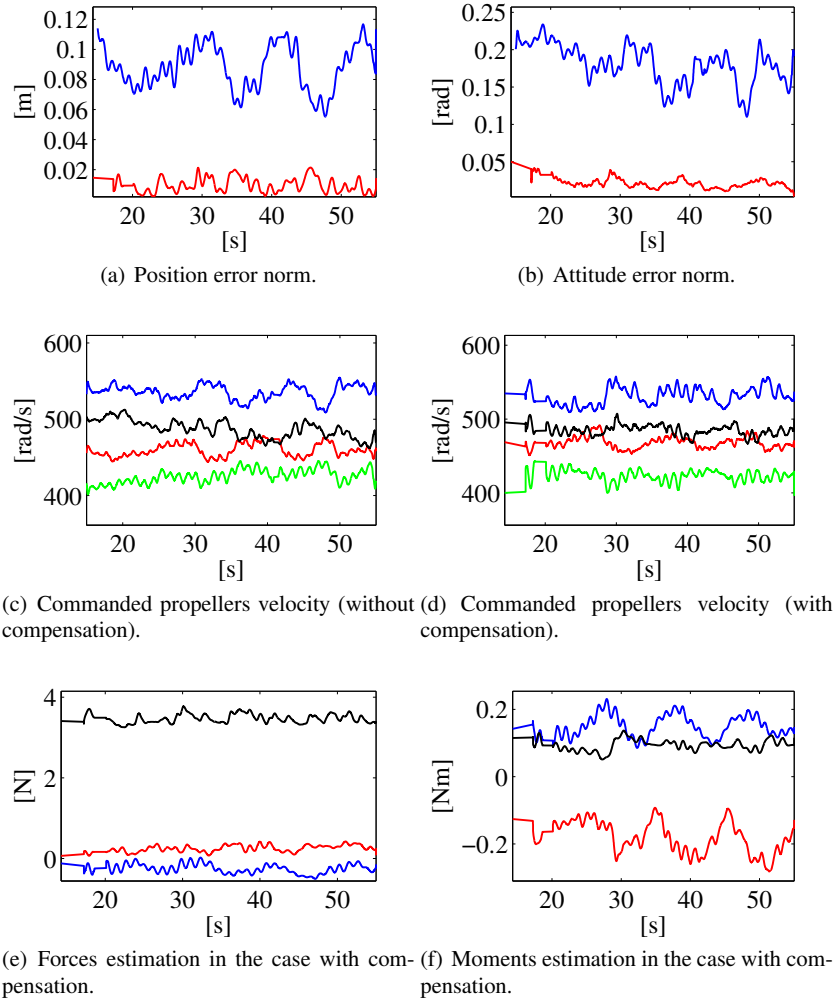
(a) Position error norm.

(b) Attitude error norm.

(c) Commanded propellers velocity (without compensation).

(d) Commanded propellers velocity (with compensation).

(e) Forces estimation in the case with compensation.

(f) Moments estimation in the case with compensation.

Fig. 104 Case study 1. Test B. Subfigure (a) shows the position error norm, while subfigure (b) illustrates the attitude error norm. In both subfigures the legend is: in blue, the case without compensation of external wrench and unmodeled dynamics; in red, the case with compensation. Subfigures (c) and (d) show the commanded propellers velocity without and with compensation, respectively. For these plots, the legend is: blue, propeller 1; red, propeller 2; black, propeller 3; green, propeller 4. In case of compensation, subfigures (e) and (f) depict the estimated forces and moments, respectively. For subfigure (e) the legend is: in blue, the estimated force along the x axis; in red, the y axis; in black, the z axis. The legend for subfigure (f) is instead: in blue, the estimated moment around the x axis; in red, the y axis; in black, the z axis.

the altitude of 1.1 m, standing persistently in front of the fan for some seconds (simulating a constant external disturbance), and then it lands. Each rectilinear path
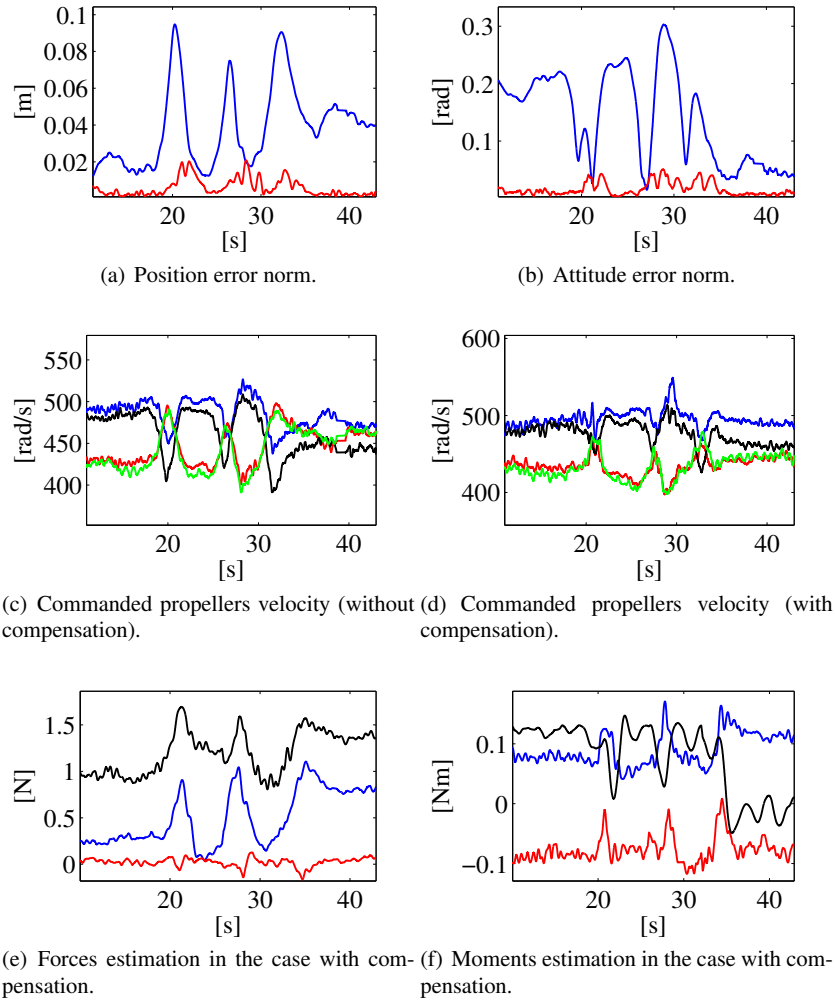
(a) Position error norm.

(b) Attitude error norm.

(c) Commanded propellers velocity (without compensation).

(d) Commanded propellers velocity (with compensation).

(e) Forces estimation in the case with compensation.

(f) Moments estimation in the case with compensation.

Fig. 105 Case study 1. Test C. Subfigure (a) shows the position error norm, while subfigure (b) illustrates the attitude error norm. In both subfigures the legend is: in blue, the case without compensation of external wrench and unmodeled dynamics; in red, the case with compensation. Subfigures (c) and (d) show the commanded propellers velocity without and with compensation, respectively. For these plots, the legend is: blue, propeller 1; red, propeller 2; black, propeller 3; green, propeller 4. In case of compensation, subfigures (e) and (f) depict the estimated forces and moments, respectively. For subfigure (e) the legend is: in blue, the estimated force along the x axis; in red, the y axis; in black, the z axis. The legend for subfigure (f) is instead: in blue, the estimated moment around the x axis; in red, the y axis; in black, the z axis.

along the vertical axis is performed at a constant speed of 0.5 m/s. The take-off and the landing phases are neglected in the plots of Fig. 105.
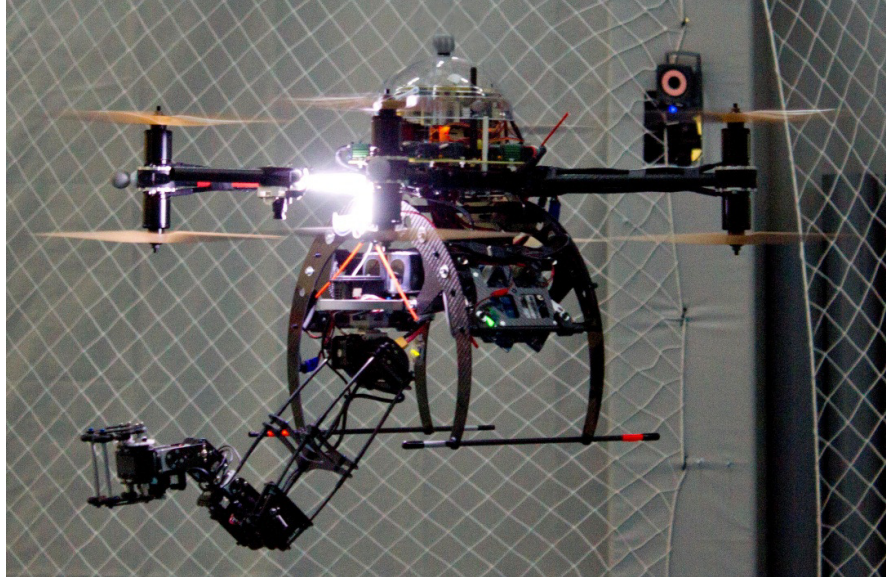
Fig. 106 The ARCAS multirotor with the attached 6-DoF manipulator.

In general, by looking at Fig. 105(a) and Fig. 105(b), it is possible to notice that the passivity-based control alone is stable even in the presence of both time-varying and constant disturbances. However, performance is poor, and it can be recovered by exploiting the compensation provided by the estimator. Fig. 105(e) and Fig. 105(f) show the estimated forces and moments in the compensation case. It is possible to notice the first passage in front of the fan at about 20 s. Notice that the estimated forces are expressed in the inertial frame, and the fan is aligned to its x axis. The second passage in front of the fan is at about 25 s. Afterward, the quadrotor stays in front of the fan from the time instant at 31 s until the landing command is given. At that point, it is possible to notice that the estimated forces are almost constant (about 0.8 N along the x axis), while the estimated moments wave due to small oscillations of the aerial platform caused by small turbulent aerodynamic effects on the aerial vehicle. This last causes also a small estimated force along the vertical axis.

The commanded propellers inputs are represented in Fig. 105(c) and Fig. 105(d).

3.2 Case study 2

The described estimator of the external wrench is now employed within an aerial manipulator device. The performance of already existing stable controller improves through the injection of the proposed estimator while keeping the stability property alive.

The chosen aerial manipulator is the ARCAS multirotor depicted in Fig. 106. The ARCAS multirotor is an eight-rotor aircraft in a coaxial configuration with a tip-to-tip wingspan of 105 cm, 13-inches propellers, a height of 50 cm and mass of 8.2 kg including the Lithium Polymer batteries and the attached robotic arm. Such robotic arm is a 6-DoF manipulator [1] whose servos are updated at 50 Hz. The first two joints give yaw and a pitch movement to the end-effector. After an elongated structure, the remaining four joints follow a sequence of the pitch, roll, pitch, and roll movement given to the end-effector. The joints are actuated by the Robotis-Dynamixel DC (MX-106, MX-64, and MX-28) servomotors. They are small, lightweight and having a geometry that facilitates the installation. They use half duplex asynchronous serial communication and allow configuring an internal PID controller. Besides, the device has an auxiliary component fixed to the landing gear hosting a counterweight that is moved on a linear slider during the manipulator operation to keep the center of gravity (CoG) of the whole system (UAV plus the arm) as close as possible to the multirotor geometric center.

The autopilot in use allows full control of all the hardware and software to integrate the robotic arm and the code used to carry out the described case study. To this aim, a Model-Based Design methodology [8] established on Simulink code generation tools that have proved to be very reliable, fast and convenient, is employed. For costly computing code, such as image processing, the vehicle has an i7 Asctec Mastermind on board. A Vicon [10] system is used as the positioning system. Vicon is running at 100 Hz, and it is only sending the position of the multirotor, as the attitude is obtained with an estimator using the IMU data.

The control architecture developed to control the described aerial manipulator effectively is detailed in [6]. To highlight the main features, it is worth recalling the four modules forming the control architecture.

- The estimator and data processing module. This module receives all the data from the onboard sensors and estimates the position, the linear velocity, the attitude, and the angular velocity of the platform. Besides, the module gets the safety operator radio references.
- The position control module. From the state of the aerial manipulator and the given references, the module takes care of the stabilization of the position of the aerial platform, providing as output the references to the module described below. This module also receives the linear compensation terms provided by the described estimator of the external wrench.
- The attitude control module. From the state of the aerial manipulator and the given references, such module stabilizes the angular part of the UAV, also sending the control signal to each of the eight motors. Furthermore, this module receives also the angular compensation terms from the described estimator of the external wrench.
- The robotic arm controller module. This module is in charge of the final checks of the references given to the arm, its deployment, retraction, and parsing the values to servo control signals. Possible self-collisions are managed at this level.
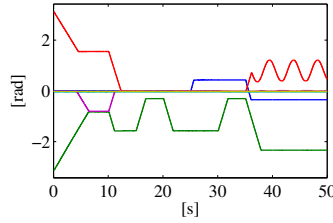
Fig. 107 Commanded joint positions of the attached arm. From the first to the sixth joint, the color legend is: blue, green, red, cyan, magenta, and olive.

In this case study, the primary control goal is to keep fixed the CoG of the UAV while the attached manipulator moves the joints along a predefined trajectory. Two tests are considered and then compared. In the former one, the UAV is controlled without injecting the compensation term from the estimator, relying in this way only on the low-level PID-based controllers of the aerial device plus the battery sliding. In the latter test, the compensation term is activated to make the multirotor aware of the movement of the joints and compensate for additional unmodelled effects. The movements of the joints of the attached manipulator are planned as depicted in Fig. 107. In detail, the manipulator starts in the retracted position and reaches a specific deploying configuration as soon as the experiment starts. Each 5 seconds, the configuration of the arm changes trying to excite its dynamics and thus the effects on the aerial platform. After six different configurations, the third joint starts to behave like a pendulum. Finally, the experiment ends. During each movement, the commanded velocity for each joint is 40 deg/s. Notice that this velocity is higher than possible velocities needed to carry out real on-site aerial manipulation tasks. Such a velocity is chosen on purpose to stress the effects of the dynamic forces induced on the aerial platform.

3.2.1 Test A.

In this test, only the basic PID control for the UAV is active, while the battery compartment moves to counterbalance the manipulator effects. The gains of the PID-based controller have been tuned in practice, such as to obtain the best experimental performance on the UAV without the robot arm.

The plots summarizing the performed experiments are depicted in Fig. 9. The position error norm of the multirotor CoG is shown in Fig. 108(a). The peaks remain relevant (about 25 cm). Fig. 108(b) illustrates the roll and pitch multirotor attitude to the inertial frame: in hovering, such angles should be null as much as possible. Given control thrust and torques are depicted in Fig. 108(c) and Fig. 108(d), respectively.

The movement of the battery on the slider mechanism is depicted in Fig. 109. The effect of this mechanism is fascinating, especially from a mechanic point of view, but alone it is not enough to compensate for the variation of the movements that a
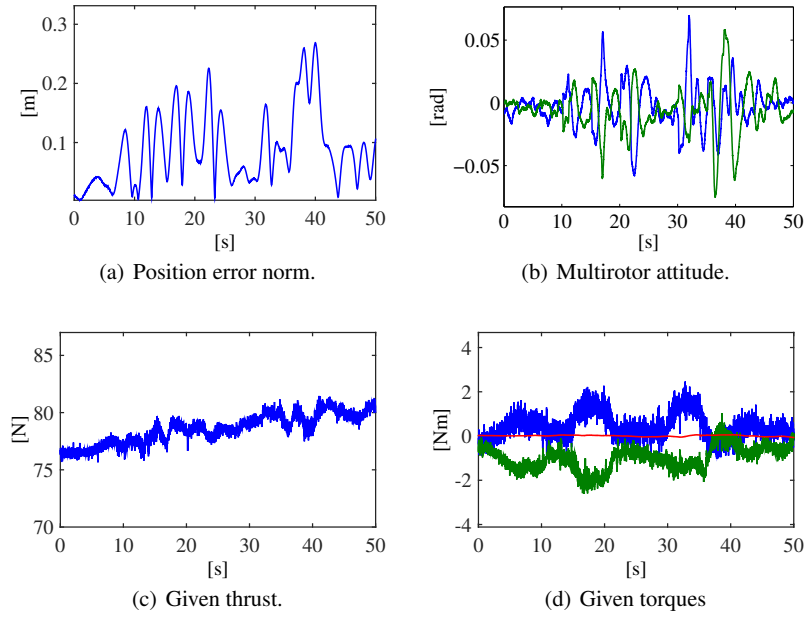
(a) Position error norm.

(b) Multirotor attitude.

(c) Given thrust.

(d) Given torques

Fig. 108 Case study 2. Test A. In this case, only the PID-based control of the multirotor and the battery compartment movement is active. Subfigure (a) shows the position error norm of the multirotor CoG. Subfigure (b) illustrates the roll (blue) and pitch(green) angles. Subfigures (c) and (d) show the given thrust and control torques given to the multirotor, respectively. The legend for Subfigure (d) is: blue, the roll component of τ_b^b; green, the pitch component and red the yaw one.
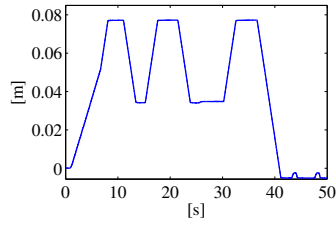

Fig. 109 Case study 2. Test A. Movement of the battery slider.

manipulator might perform. This limitation of the introduced mechanism justifies the injection of the external wrench estimation.

3.2.2 Test B.

In this test, the PID controller is sustained by the estimator of the external wrench. It is straightforward to recognize the performance increase: without re-tuning the PID controller again, it is possible to mount a robot arm under a UAV to play as an aerial manipulator.

About the parameters of the estimator, the chosen degree is $r = 2$, while the gains are tuned to $\mathbf{K}_1 = \mathrm{diag}\,(14,\ 14,\ 16,\ 24,\ 24,\ 4.5)$ and $\mathbf{K}_2 = \mathrm{diag}\,(3.5,\ 3.5,\ 4,\ 6,\ 6,\ 1.39)$. As visible from Fig. 110(a), the error norm about the hovering position of the aerial vehicle is lowest than the previous test (about 6 cm as maximum). To maintain as much as possible the CoG of the UAV close to the commanded hovering position, the aerial vehicle has to perform quick movements to counterbalance both the statics and the dynamics of the moving manipulator arm. This is highlighted in the attitude roll and pitch behavior depicted in Fig. 110(b), and in the total commanded thrust and torques shown in Fig. 110(c) and Fig. 110(d), respectively. Battery movement of the slider is comparable to the above test. The estimated external forces and moments are represented in Fig. 110(e) and Fig. 110(f), respectively.

About this last time histories, two considerations can be carried out. First, the initial estimator conditions are null, as underlined within Section 2. However, the estimating process starts when the aerial vehicle takes off. In the represented plots, instead, the starting time for the task is when the robotic arm starts to be deployed. Second, it is possible to observe a slow drift-like effect in Fig. 110(e) concerning the z component of the estimated external forces. This is mainly due to a recirculation wind flow due to the indoor arena and generated in the time frame of the experiment by the eight propellers.

Finally, considering a comparison between the averages of the position error norms of the multirotor CoG in each of the case studies (Test A: 10.4 cm; Test B: 2.25 cm; see also Fig. 111), it is evident the benefit of the estimator improving the performance of the UAV control.

4 Conclusion

A decentralized approach to control an aerial manipulator has been presented. The aerial device has seen as a separate entity from the robotic manipulator. From a control viewpoint, the easiest way may be designing (and tuning) a proper controller for the aerial vehicle, and a separate one for the arm. This chapter shows how it is possible to combine this device efficiently by injecting a further action into the existing controller of the UAV. This control action comes out from an estimator of the external wrench of the aerial vehicle. Through experimentally case studies, it has been seen how it is possible to apply this concept to different existing controllers without altering their previous tuned gains, as well as its applicability to aerial manipulators.
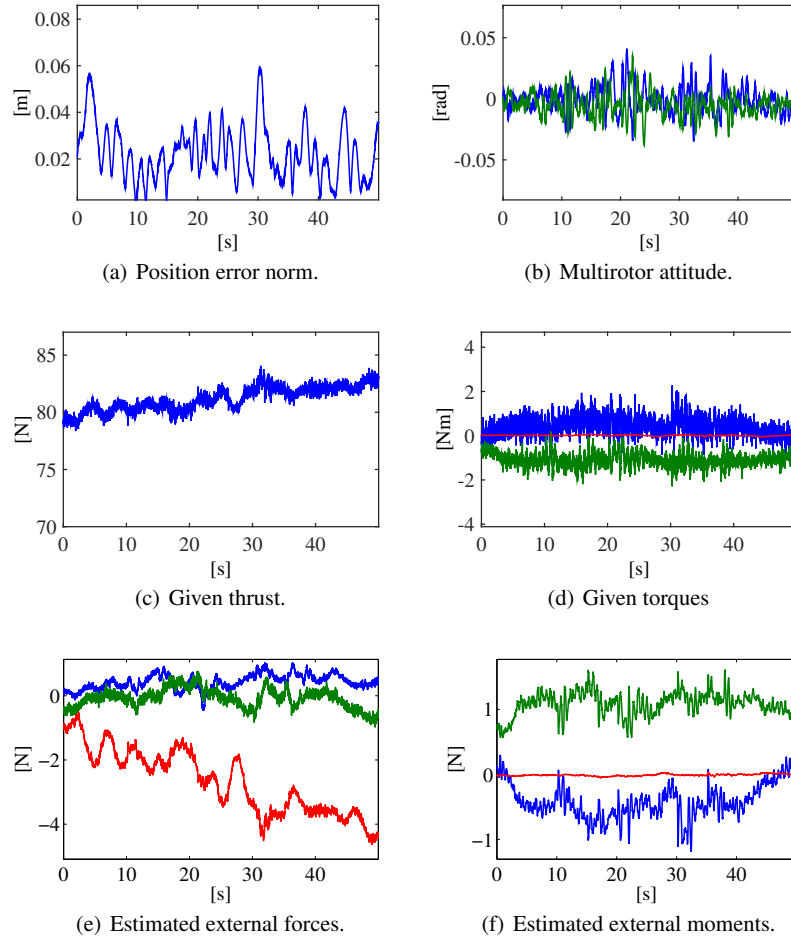
(a) Position error norm.

(b) Multirotor attitude.

(c) Given thrust.

(d) Given torques

(e) Estimated external forces.

(f) Estimated external moments.

Fig. 110 Case Study 2. Test B. The estimation is now injected into the controller. Subfigure (a) shows the position error norm of the multirotor CoG. Subfigure (b) illustrates the roll (blue) and pitch (green) angles. Subfigures (c) and (d) show the given thrust and control torques, respectively. The legend for Subfigure (d) is: roll component of τ_i in blue, the pitch is in green, the yaw in red. Subfigures (e) and (f) illustrate the unfiltered estimated external forces and moments, respectively. Subfigure (e) depicts the estimated force along x (blue), y (green) and z (red) axes of body frame. The legend for Subfigure (f) is: the roll component of the estimated external moments is in blue, the pitch is in green and the yaw in red.
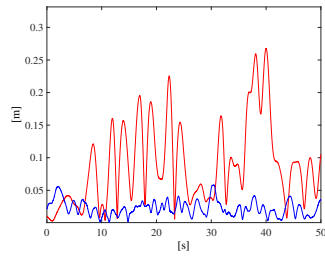
Fig. 111 Case study 2. Comparison between the position error norm of test A (red) and B (blue).

References

1. R. Cano, C. Pérez, F. Pruaño, A. Ollero, and G. Heredia. Mechanical design of a 6-DOF aerial manipulator for assembling bar structures using UAVs. In *2nd RED-UAS 2013 Workshop on Research, Education and Development of Unmanned Aerial Systems*, 2013.

2. F. Huber, K. Kondak, K. Krieger, D. Sommer, M. Schwarzbach, M. Laiacker, I. Kossyk, S. Parusel, S. Haddadin, and A. Albu-Schaffer. First analysis and experiments in aerial manipulation using fully actuated redundant robot arm. In *2013 IEEE/RSJ International Conference on Intelligent Robots and Systems*, pages 3452–3457, Tokyo, J, 2013.

3. A.E. Jimenez-Cano, J. Martin, G. Heredia, A. Ollero, and R. Cano. Control of an aerial robot with multi-link arm for assembly tasks. In *IEEE International Conference on Robotics and Automation*, pages 4916–4921, Karlsruhe, D, 2013.

4. F. Ruggiero, J. Cacace, H. Sadeghian, and V. Lippiello. Impedance control of VToL UAVs with a momentum-based external generalized forces estimator. In *2014 IEEE International Conference on Robotics and Automation*, pages 2093–2099, Hong Kong, C, 2014.

5. F. Ruggiero, J. Cacace, H. Sadeghian, and V. Lippiello. Passivity-based control of VToL UAVs with a momentum-based estimator of external wrench and unmodeled dynamics. *Robotics and Autonomous Systems*, 72:139–151, 2015.

6. F. Ruggiero, M.A. Trujillo, R. Cano, H. Ascorbe, A. Viguria, C. Peréz, V. Lippiello, A. Ollero, and B. Siciliano. A multilayer control for multirotor UAVs equipped with a servo robot arm. In *2015 IEEE International Conference on Robotics and Automation*, pages 4014–4020, Seattle, WA, USA, 2015.

7. Fabio Ruggiero, Jonathan Cacace, Hamid Sadeghian, and Vincenzo Lippiello. Passivity-based control of vtol uavs with a momentum-based estimator of external wrench and unmodeled dynamics. *Robotics and Autonomous Systems*, 72:139 – 151, 2015.

8. D. Santamaria, F. Alarcon, A. Jimenz, A. Viguria, M. Béjar, and A. Ollero. Model-based design, development and validation for UAS critical software. *Journal of Intelligent & Robotic Systems*, 65(1–4):103–114, 2012.

9. B. Siciliano, L. Sciavicco, L. Villani, and G. Oriolo. *Robotics: modelling, planning and control*. Springer Verlag, 2009.

10. VICON. Vicon Motion Systems. Ltd.